THE ASTROPHYSICAL JOURNAL, 368:474–485, 1991 February 20

AN INFRARED ANALYSIS OF PUPPIS A

RICHARD G. ARENDT,[1] AND ELI DWEK
Laboratory for Astronomy and Solar Physics, NASA/Goddard Space Flight Center
AND
ROBERT PETRE
Laboratory for High Energy Astrophysics, NASA/Goddard Space Flight Center
Received 1990 April 9; accepted 1990 August 8

ABSTRACT

We have completed a quantitative analysis of the infrared emission of the supernova remnant (SNR) Puppis A as seen by the *Infrared Astronomical Satellite* (*IRAS*). We estimate physical parameters of the remnant (and the surrounding interstellar medium), including density, mass, temperature, and age. The infrared spectrum of Puppis A is fit by models of thermal emission from interstellar dust grains which have been swept up into the SNR where they are collisionally heated by the shocked gas. We find evidence of an enhanced abundance of very small grains in the interstellar medium near Puppis A, and evidence of their destruction by the advancing blast wave.

Subject headings: infrared: sources — interstellar: grains — nebulae: individual (Puppis A) — nebulae: supernova remnants — radiation mechanisms

I. INTRODUCTION

The middle-aged supernova remnant Puppis A has long been studied at radio, optical, and X-ray wavelengths. Its high surface brightness in these spectral regimes, and its generous angular size have made it a popular target of many varied investigations. In the wake of the *Infrared Astronomical Satellite* (*IRAS*) mission (Neugebauer *et al.* 1984), Puppis A has been found to be a prominent IR source as well. In this paper we present the first quantitative analysis of the infrared (IR) emission of Puppis A. A qualitative examination of the morphology of the remnant and its surroundings at infrared, X-ray, radio, and optical wavelengths was presented by Arendt *et al.* (1990; hereafter Paper I). Comparison of the IR emission from Puppis A with emission at the other wavelengths revealed a good spatial correlation between the IR and the X-ray emission. No such correlation was found between the IR and radio or optical emission from the remnant. We therefore believe that a negligible amount of line and thermal emission from dense filaments contributes to the observed IR flux densities of Puppis A. The contribution of the radio synchrotron emission, when extrapolated to the infrared with a spectral index of $\alpha = -0.53$ (Milne 1971), to the *IRAS* bands is negligible as well. All this suggests that the IR emission from the supernova remnant (SNR) arises from swept-up interstellar dust that is collisionally heated by the X-ray emitting plasma. Outside the SNR cavity, the IR emission arises from dust heated by ambient starlight. This emission plays an important role in studying the interaction of the remnant with the ambient interstellar medium (ISM). In Paper I we identified three distinct clouds in the *IRAS* images, previously identified by radio spectral-line observations (Dubner and Arnal 1988) and an optical image (Elliot, Goudis, and Meaburn 1976) of the region. Two are interacting with Puppis A, while the third lies much closer to us along the line of sight.

In this paper we present a quantitative analysis of the IR emission from the remnant and its surrounding medium. Since the IR emission is contaminated by emission from various sources along the line of sight, this analysis requires careful attention to the background emission across the region of Puppis A. Subtraction of this background emission component from the image is complicated by the fact that it exhibits spatial variations across the remnants. The data reduction, and particularly the background subtraction procedures are described in detail in § II. The background-subtracted images can then be used to determine the IR fluxes of the entire SNR and specific regions of interest inside and outside the remnant. The integrated emission from the remnant is used to estimate various properties such as the ISM density, and the mass, radius, and age of the SNR using a generic description of the dust (§ III). In § IV we describe the procedure we used to develop physical models of the IR emission. Briefly, this entails using estimates of plasma temperatures and densities to calculate the IR spectrum of dust immersed in the plasma. We can derive detailed information on the grain size distribution from modeling the IR emission. The short wavelength IR emission arises primarily from stochastically heated small grains. Therefore, if the initial grain size distribution is known, the intensity of the short-wavelength emission can tell us the amount of grain destruction that has occurred since that localized region of the remnant has been shocked. From the IR emission we can also derive the mass of gas and dust, the thickness of the emitting region, and estimates of the length of time that the dust has been subjected to sputtering within the SNR. In § V we apply our physical models to specific regions of interest inside the remnant for which there are constraints on the gas temperature and density from the X-ray analysis (Szymkowiak 1985). The analysis of localized regions outside the remnant is also of particular interest in Puppis A, since one of these regions (the "east cloud") is believed to be interacting with the remnant. Analysis of the IR emission from this cloud and from the interaction region inside the remnant will provide information about the dust processing behind the shock. The results of both the generic dust model and the physical models are discussed in § VI. The final section (VII) recaps the highlights of this work.

[1] National Research Council/Resident Research Associate.

II. DATA ANALYSIS

In Paper I we restricted ourselves to the morphological analysis of the remnant. The results derived were qualitative, and not seriously affected by the presence of background emission in the IR data. However, to obtain quantitative results, the background emission must be removed, and the data at all wavelengths should be compared at the same resolution. This section describes the procedures we followed to prepare the data for quantitative analyses.

The infrared data used here were collected as part of the all-sky survey completed by *IRAS* (Neugebauer *et al.* 1984). The data from each of the scans across the region of Puppis A have been processed into intensity maps (units of W m^{-2} sr^{-1}) in each of the four *IRAS* bands (nominally at 12, 25, 60, and 100 μm) using the standard co-adding techniques employed at the Infrared Processing and Analysis Center (IPAC). Each image is 2° on a side with pixels of 15″ at 12 and 25 μm, 30″ at 60 μm, and 60″ at 100 μm. For comparison, the images from the 12, 25, and 60 μm bands were gridded onto 60″ pixels before subsequent processing, so that all images have the same size and scale. To determine whether variation in different quantities across the image are physically meaningful, we estimated the resolution of each of the co-added images. The resolution in each image depends on the shape and size of the effective beam of the band, and on the directions of the satellite's scans across the region. The resolution was estimated by Gaussian fits to the bright pointlike source IRAS 08247−4223, which appears at $\alpha = 8^h24^m43^s.1$, $\delta = -42°23'10''$ in all four bands. All the scans across the region of Puppis A were nearly parallel, which resulted in a fairly well-behaved beam. The resolution estimated in each band is listed in Table 1.

The images created through the co-addition processing have a uniform bias level removed so that the zero intensity level is arbitrarily set. In addition, IPAC normally applies a field-flattening process to the co-added images they produce. This process is intended to remove large-scale gradients of the background. Comparison of these flattened images with a set of images that were not flattened revealed that the background removed was relatively smooth with no structure on a scale of less than about 1°. However, the gradient of the removed background seemed to be influenced over much of each image by the bright emission (centered at roughly $\alpha = 8^h21^m.5$, $\delta = -41°55'$) to the north of Puppis A. This emission is related to the association Puppis R1 and its surrounding reflection nebula (van den Bergh and Herbst 1975; Herbst 1975). Because the reflection nebula does not appear to extend over most of the field (though we note that the IR emission is much more extended than the optical emission), we believe the gradient of the background had been overestimated due to the presence of this strong source on the edge of the field. Therefore, the flattened versions of the images were rejected and further work used the co-added images which were not flattened by the IPAC processes.

TABLE 1

IRAS RESOLUTION ESTIMATED FROM IRAS 08247−4223

Wavelength (μm)	Full-Width Half-Maximum	Position Angle
12.....	4.'71 × 1.'76	118°
25.....	4.74 × 1.63	118
60.....	5.35 × 2.29	115
100.....	5.60 × 4.37	118

Ideally, we would like to remove the background emission by modeling each source of emission along the line of sight. Unfortunately, despite the identification of several distinct background objects (see Paper I), we do not know their structure or spectra well enough to extrapolate their emission where they overlap Puppis A. Furthermore, there is still a great deal of low-level, small-scale variations in the "dark" area of the images. Modeling these background variations in detail is beyond our abilities. Therefore, we have removed a smooth (large-scale) emission component which represents the background emission over the area of the SNR. Puppis A is located amid a "ridge" of IR emission which is distinct from the general Galactic disk emission (Paper I). Together the ridge and the Galactic disk contribute the bulk of the large-scale background emission. Both these features produce emission with an intensity gradient toward the Galactic plane. The curvature of the background over the area of the SNR is small compared to the small-scale variations seen in the rest of the images. Therefore, we have used a tilted plane to model the background emission across Puppis A. The slope, orientation, and offset of the planar background were allowed to vary to find the best fit to the emission from the narrow regions just outside the apparent IR boundaries of Puppis A. (These regions were indicated in Fig. 5 of Paper I.) The resulting background-subtracted images appeared good at 25 and 60 μm in that the apparent edges of the SNR were at or near zero, and regions of the images without obvious sources were at a fairly uniform level near zero. The gradients of the backgrounds removed from these two bands were 5.89 and 5.36×10^{-8} W m^{-2} sr^{-1} $degree^{-1}$ in position angles of 4.°7 and 20.°4 measured eastward from north, respectively. The backgrounds derived for the 12 and 100 μm bands were much steeper, however, and resulted in background levels which were not uniform across the images. The cause of these steeper backgrounds appeared to be nearby sources to the east and north (the east cloud and the reflection nebula) that are relatively more prominent with respect to the general background in these bands and contaminate the regions selected to define the background. Better results were achieved at 12 and 100 μm by using the average of the 25 and 60 μm planar backgrounds. This average plane had a gradient of 5.61×10^{-8} W m^{-2} sr^{-1} $degree^{-1}$ at a position angle of 12.°3. The level of this background had to be adjusted downward by a bias of 5.5×10^{-8} W m^{-2} sr^{-1} to give a suitable zero level in the resulting background-subtracted images at 12 and 100 μm. This adjustment was determined independently for the 12 and 100 μm images by requiring that the empty region adjacent to the southeast edge of Puppis A was at or below zero. (Note that the spectrum of the dominant background emission in the region of Puppis A is not accurately represented by the background adjustments described above, since an unspecified flat background level had already been removed in the zero-level bias of the original co-added images.) Contour maps of these background subtracted images were presented in Paper I.

Our neglect of the background curvature appears as negative-emission regions in the northeast and southwest corners of the images, where the true background is falling below the assumed planar background which is tangent to it at the center of the image. However, the dominant errors in the background fitting across Puppis A itself arise from our inability to account for the small-scale variations. These errors can

be gauged in two ways. One is that all regions within the boundaries of the SNR should show positive emission since no absorption is expected at these wavelengths. Therefore, any negative regions within the remnant indicate an oversubtraction of the background, at least in that local area. The largest negative deviations within a rectangular region including the entire SNR are -7.7, -3.1, -4.9, and -5.4×10^{-8} W m^{-2} sr^{-1} in the 12, 25, 60, and 100 μm bands, respectively. The other means of assessing the errors involves checking how closely the regions selected to determine the background were reduced to a constant zero level. The rms dispersions about a mean of zero of the pixel intensities in the selected regions are 1.2 and 2.2×10^{-8} W m^{-2} sr^{-1} in the 25 and 60 μm bands. The maximum deviations in these bands are 3.7 and 5.9×10^{-8} W m^{-2} sr^{-1}. This method is not applicable to the 12 and 100 μm bands, since the background used in these bands was obtained by a different method, as described above. As a convenient means of describing these results, we can adopt nominal "3 σ" errors of 7.5, 3.5, 5.5, and 5.5×10^{-8} W m^{-2} sr^{-1} for the 12, 25, 60, and 100 μm bands, respectively. We stress that these values are not statistically determined; however, they do provide a good description of the data, based on analysis of the regions which we can examine in a proper statistical method and based on the general appearance of what we believe are significant features in the images. At 60 μm all of the emission from the remnant appears at levels greater than "3 σ"; at 25 and 100 μm only about half of the SNR shows emission above the "3 σ" level; and at 12 μm only a small area of emission at the location of the eastern knot approaches the "3 σ" level.

For comparison between images in the different bands, additional images at 12 and 25 μm were created which were smoothed to the resolution of the 60 μm image. These images were used for the following analysis, since the better resolution of the shorter wavelength bands could introduce spurious results, particularly where steep gradients in brightness are encountered, such as along the northeast edge of the SNR. We chose not to smooth to the resolution of the 100 μm images to avoid losing too much of the spatial information of the shorter wavelength images. This leaves the possibility of finding spurious results if detailed comparisons are made between the 100 μm and other images.

III. A GENERIC DUST MODEL

a) *Flux Densities and Dust Color Temperatures*

The flux densities were measured in each wavelength band by integrating over regions within the zero-level contours. However, since the emission of the SNR merges with that of confusing sources in some directions, we excluded confusing sources by additionally using the 5.5×10^{-8} W m^{-2} sr^{-1} contour of the 60 μm emission (excluding the region of the tail, $\delta \lesssim -43°15'$) as a template. This extent, as defined by the 60 μm emission, closely resembles that of Puppis A in the radio and X-ray regimes, except in the southeast quadrant of the SNR where radio and X-ray data show a wider extent of faint diffuse emission. The resulting fluxes were converted to flux densities (listed in Table 2) using the nominal *IRAS* bandwidths of 13.48, 5.16, 2.58, and 1.00×10^{12} Hz, at 12, 25, 60, and 100 μm respectively. To derive a dust temperature from the fluxes, the emissivity of the dust must be known. At the moment it is sufficient to adopt a "generic dust" model which is characterized by power-law emissivity. Our generic dust is characterized by an emissivity $\propto \lambda^{-1.5}$ and a mass-absorption coefficient, κ, with optical constants given by Draine and Lee (1984). This generic dust model represents a mixture of graphite and silicate dust properties. Given the emissivity law, the ratios of flux densities in adjacent bands i, and j were used to derive initial color temperatures T_{ij}. (Throughout this work, we shall use i and $j = 1$, 2, 3, and 4 to indicate the *IRAS* bands at 12, 25, 60, and 100 μm respectively.) These color temperatures were then used to derive the color-correction factors in each band (*IRAS Explanatory Supplement* 1985). The color-corrected flux densities are listed in Table 2. The errors for the flux densities were generously estimated by assuming that the "3 σ" deviations derived in § II could occur in the same direction across the entire extent of the SNR. At 12 μm we only present an upper limit of 100 Jy (the 12 μm "3 σ" deviation times the solid angle of the SNR), since the only location across Puppis A which exhibits any 12 μm emission is the eastern knot, and even that is faint and confused.

TABLE 2

INTEGRATED PARAMETERS OF PUPPIS A

Wavelength (μm)	Measured Flux Density (Jy)	Color-Corrected Flux Density (Jy)	Temperature (K)
12.....	<100	<100	($\sim$120)
25.....	245 ± 120	291	65^{+12}_{-7}
60.....	1195 ± 350	1250	44^{+170}_{-11}
100.....	1265 ± 990	1250	

We found dust color temperatures of $T_{12} \approx 120$ K, $T_{23} = 65^{+12}_{-7}$ K, and $T_{34} = 44^{+170}_{-11}$ K, where the range for each temperature reflects the "3 σ" uncertainties of the flux densities. The temperature derived from the 12 and 25 μm flux densities (T_{12}) was determined only from the emission of the east knot, and thus may not represent the rest of the SNR. The differences between the derived color temperatures using different *IRAS* bands are expected since the temperature of a grain is a function of its size, and since the temperatures of smaller grains can fluctuate significantly (see Dwek 1986, 1987). Thus, the dust grains within a SNR exhibit a range of fluctuating temperatures. All SNRs visible in the IR (except a few of the youngest) exhibit similar variations between the color temperatures derived from different bands (Arendt 1989). We also checked for spatial variations of the color temperatures on scales of 7′ across the remnant. We found no variations of T_{23} or T_{34} which exceeded the expected range due to uncertainties in the measured flux densities.

Temperatures can be derived for other sources in the field, however these are not as reliable as those for the SNR, since no attempt was made to make the background subtraction accurate away from Puppis A itself. With this caveat, the temperatures derived for the east cloud are $T_{12} = 250$ K, $T_{23} = 65$ K, and $T_{34} = 23$ K; for the tail $T_{12} = 240$ K, $T_{23} = 65$ K, and $T_{34} = 33$ K; and for the reflection nebula $T_{12} = 200$ K, $T_{23} = 60$ K, and $T_{34} = 28$ K. The color temperatures for the east cloud and the tail are very similar to those derived for IR cirrus clouds (Low *et al.* 1984; Verter *et al.* 1990), which are heated by the interstellar radiation field (ISRF). The color temperatures for the IR emission around the Puppis R1 association are similar to those found for other reflection nebulae (see Luan *et al.* 1989, and references therein).

The total infrared flux received from Puppis A is $F_{IR} = 1.1$

$\times 10^{-7}$ ergs s^{-1} cm^{-2}. This is determined by adding the fluxes from each of the *IRAS* bands, and correcting for the fact that only $\sim 55\%$ of the total flux from blackbody sources between about 26 and 100 K is detected in the *IRAS* bands. The correction was derived from filter parameters listed in the *IRAS Explanatory Supplement* (1985), and is consistent with the correction used by Casoli *et al.* (1986). We estimate the uncertainty in the IR flux to be on the order ~ 2.5. The total IR flux we find here is $\sim 60\%$ higher than that estimated by Dwek *et al.* (1987) through fitting a single-temperature generic dust spectrum to be independently measured *IRAS* flux densities.

b) *Global Remnant Properties*

The infrared emission from Puppis A as a whole can be used to estimate various global or average physical properties of the remnant and the surrounding ISM. Assuming the distance to Puppis A is reasonably well-determined, the radius and IR luminosity of the SNR are found from basic geometry. We can estimate the mass of the dust (M_d) responsible for the IR emission from the relation:

$$4\pi d^2 S_\nu = 4 M_d \kappa_\nu \pi B_\nu(T_d) , \quad (1)$$

where d is the distance to the SNR, S_ν is the flux density, κ_ν is the mass-absorption coefficient, and $B_\nu(T_d)$ is the blackbody emissivity at a dust temperature T_d. The mass of gas, M_g, is simply related to the dust mass by a dust-to-gas mass ratio, Z_d. Inside the remnant this ratio may be modified from its preshock value by sputtering. The gas mass divided by the volume of the SNR yields the mean initial density (n_0) within the volume now occupied by the SNR. For strong adiabatic shocks, the density of the IR emitting gas will be given by $n \approx 4\ n_0$. The temperature of a collisionally-heated dust particle of radius a is a simple function of gas temperature and density (e.g., Dwek 1987) which can be inverted to give the gas temperature in terms of the other quantities as:

$$T_6 = 7.33 \times 10^{-6} T_d^4 n^{-2/3} a^{2/3} , \quad (2)$$

where T_6 is the gas temperature in units of 10^6 K, and a is given in μm. Equation (2) assumes that all electrons are stopped in the grains, and is strictly applicable to gas temperatures below $\lesssim 10^7$ K, and grain sizes larger than 0.05 μm (see Fig. 3 of Dwek 1987). With estimates of the remnant radius, gas temperature, and initial density, we can apply the standard Sedov phase relations to solve for the age (t) of the SNR and the initial energy (E).

Remnant parameters derived through this approach are presented in Table 3. The first column in the table is the dust temperature, T_d, taken to be equal to $T_{34} = 44$ K. Some of the derived results can be strong functions of dust temperature ($\sim T_d^8$). Therefore to illustrate the sensitivity of our results to uncertainties in T_d, we calculated parameters using ± 4 K variations in this quantity. While the actual T_d may well be outside the range of 44 ± 4 K, it is very unlikely to lie near the extremes of the formal range quoted in Table 2, since such values (particularly at the high-temperature end) would lead to a very peculiar spectrum which could not be a sum of blackbody spectra, and also these extreme temperatures would yield improbable derived parameters. The second column is the distance to the remnant, taken to be 2 kpc. The derived quantities are never more sensitive to the assumed distance than d^3. Even so, we allowed for ± 0.4 kpc variations in this quantity as well. The radius of the remnant was derived from the distance by assuming a mean angular radius of 28′. The total infrared luminosity represents the total IR flux scaled by the adopted distance of the remnant. To derive the dust mass we have normalized the mass absorption coefficient to $\kappa = 120\ cm^2\ g^{-1}$ at 60 μm. We made these calculations using 60 μm data since the flux density is more reliable than that at 100 μm, and it should still be unaffected by the transient heating and emission of small grains which strongly influences the 12 and 25 μm flux densities. The gas mass was derived from that of the dust by assuming an average interstellar dust-to-gas mass ratio of 0.0077, ie., we neglected the effect of grain destruction in the shocked gas. (This effect will be considered in detail in the following sections.) We assumed that the ejected mass of the progenitor star is small compared to the mass of the swept up interstellar medium, and derived the ambient gas density, n_0, from M_g for a mean molecular weight of 1.26. The shell density, n, is simply $4n_0$, its adiabatic value immediately behind the shock. The gas temperature was then derived by using equation (2) for an average grain size of 0.1 μm. The remnant age, t, and explosion energy E, were derived from the Sedov solution.

The results derived from our adopted $T_d = 44$ K and $d = 2.0$ kpc are listed on the first line of Table 3. The rest of Table 3 illustrates that errors in the dust temperature will most strongly affect the derived gas temperature, masses, and densities, while errors in the distance will affect the explosion energy, luminosity, and masses.

IV. THE PHYSICAL MODEL FOR THE IR EMISSION

The infrared flux density (S_λ) from a region of volume V is given by (e.g., Dwek 1986):

$$S_\lambda = (4\pi d^2)^{-1} \sum_i \int_0^\infty n_i(a) V 4\pi a^2 Q_{i,\lambda}(a) \times \left[\int_0^\infty \pi B_\lambda(T_d) G_i(a, T_d) dT_d \right] da , \quad (3)$$

where $n_i(a)$ is the number density of grains of composition i and size a, $Q_{i,\lambda}(a)$ is the emissivity for grains of composition i and size a, and $G_i(a, T_d)$ is the probability of finding a grain of composition i and size a at the temperature T_d. A physical

TABLE 3

RESULTS FROM GENERIC DUST MODEL AS FUNCTIONS OF DISTANCE AND DUST TEMPERATURE[a]

T_d (K)	d (kpc)	R_s (pc)	L_{IR} ($L_\odot$)	M_d ($M_\odot$)	M_g ($M_\odot$)	n_0 (cm^{-3})	n (cm^{-3})	T_6 (10^6 K)	t (yr)	E (10^{51} ergs)
44	**2.0**	**16**	**14000**	**0.25**	**33**	**0.060**	**0.24**	**15**	**6000**	**0.56**
44	1.6	13	8600	0.16	21	0.074	0.30	13	5200	0.33
44	2.4	20	19000	0.36	47	0.045	0.18	19	6700	1.0
40	2.0	16	14000	0.43	56	0.11	0.42	7.2	8600	0.50
48	2.0	16	14000	0.16	21	0.040	0.16	28	4400	0.69

[a] The preferred values are in boldface type.

model of the infrared emission therefore requires knowledge of the grain size distribution and composition, and of the flux of particles/photons that heat the dust and determine the function G_i. Inside the remnant, the temperature probability distribution $G_i(a, T_d)$ is calculated, assuming that the dust is collisionally heated. Therefore, $G_i(a, T_d)$ is determined by the temperature and density of the plasma in which the dust is immersed. Outside of the SNR the gas is much cooler, and the dust is primarily heated by the ambient ISRF. Qualitatively, $G_i(a, T_d)$ behaves similarly for radiative heating as for collisional heating. Small grains cool rapidly between collisions and thus have high probabilities of being found at low temperatures, but they also have low heat capacities which creates a significant high-temperature tail on $G_i(a, T_d)$. For larger grains there is less cooling between collisions, and individual collisions have smaller effects upon the dust temperatures, which generally remain near their equilibrium values. We used the approximation $G_i(a, T_d) = \delta(T - T_{eq})$, for grains large enough that the FWHM of $G_i(a, T_d)$ was less than 15% of the equilibrium temperature T_{eq}. For collisionally heated dust this limiting grain size is ~ 0.05 μm, whereas for dust heated by the ISRF this grain size is 0.02 μm.

From the comparison of the theoretically calculated IR flux density, S_λ, with the observations, we can derive the dust mass and the physical dimension of the emitting region along the observer's line of sight. The infrared flux density is proportional to $n_d V/d^2$, where n_d is the number density of dust particles in the emitting region. For a given distance and grain model, $n_d V$ is simply related to the dust mass. The total mass of shocked gas is simply derived from $M_g = M_d/\delta Z_d$, where Z_d is the dust-to-gas mass ratio, and the δ is the dust depletion caused by sputtering, defined as the ratio of the present dust mass to the initial dust mass. The volume V of the emitting region is $\Omega\, d^2 L$, where Ω is its angular size (in sr) and L is its linear dimension along the line of sight. The observations will therefore yield the value of the column density $n_d L$ (or equivalently nL if the dust-to-gas mass ratio is known) independent of the adopted distance to the remnant. With n constrained by the X-ray observations and the dust temperature, the physical model will yield the value of L, the thickness of the emitting region. Finally, the total IR luminosity from each region is simply the integral of the modeled flux density $L_{IR} = 4\pi d^2 \int S_\nu d\nu$, and is largely insensitive to the details of the dust model.

In modeling the dust we adopted the Mathis, Rumpl, and Nordsieck (1977; hereafter MRN) dust model which consists of a mixture of bare silicate and graphite grains with optical constants given by Draine and Lee (1984) and Draine (1987). For the grain size distribution, we adopted the functional form proposed by MRN, i.e., $n_i(a)da \sim a^{-3.5}\, da$ for $a_{min} < a < a_{max}$. Generally, we took $a_{min} = 3$ Å (Draine and Anderson 1985) and $a_{max} = 0.25$ μm (MRN); in the rest of this paper we refer to this as an "extended" MRN or "eMRN" grain size distribution. In some cases we allowed the possibility of a break to a steeper power-law distribution for the sizes of the smaller grains ($a < a_b$); we refer to distributions with such an enhanced population of very small grains as "eMRN + VSG" distributions. Draine and Anderson (1985) found this sort of enhancement of small grain abundances necessary for modeling the emission from infrared cirrus clouds. The depletion of the various refractory elements into dust can vary in different regions of the ISM. In this paper, we adopted a dust-to-gas mass ratio from the models of Draine and Lee (1984), and find $Z_{graphite} = 0.0029$ and $Z_{silicate} = 0.0048$, giving a total dust-to-gas mass ratio of $Z_d = 0.0077$. Comparing to the average solar elemental abundances (Cameron 1982), these ratios imply that $\sim 75\%$ of the carbon and 96% of the Mg, Si, and Fe is contained in grains.

The size distribution of a population of dust particles that has been subjected to thermal sputtering is given by $n_i'(a') = n_i(a)$, where $n_i(a)$ is the original power-law distribution of grain sizes, and $a' = a - \Delta a$, where Δa is the change in the grain radius due to sputtering. Sputtering was assumed to be independent of initial grain size, so that all grains within a hot gas of density n are after τ years reduced in size by an amount Δa given by (Draine and Salpeter 1979):

$$\Delta a(\text{Å}) = \frac{n(\text{cm}^{-3})\tau(\text{yr})}{200}\,. \tag{4}$$

Grains were assumed to be destroyed if their sizes became less than 3 Å. The dust depletion (δ) can be calculated analytically from Δa for any grain size distribution of interest.

If Δa can be determined from the observations, then equation (4) will yield the length of time the dust particles have been subjected to sputtering in a given parcel of gas. This time will be about equal to the time since the gas was swept up by the shock, and will therefore be a strict lower limit to the age of the remnant.

V. APPLICATIONS OF THE PHYSICAL MODEL

Using the physical model described above, we have modeled the emission from a cloud near Puppis A, from several localized regions of the remnant, and from the entire SNR.

The east cloud, a region outside the remnant (see Fig. 1), is in the process of being swept up by Puppis A, as evidenced by its proximity to the remnant and the morphological correlations between the cloud and the SNR (see Paper I). If we determine the nature (i.e., size distribution) of the dust in the cloud, then we have an accurate picture of the initial characteristics of the dust *before* it is processed by the SNR. Thus, we first modeled

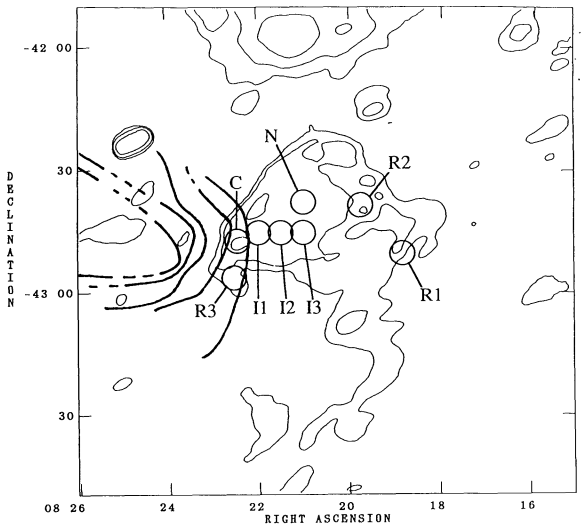

FIG. 1.—Contour map of Puppis A and its surroundings at 60 μm (levels are at 5.5, 16.5, and 66 $\times$ 10^{-8} W m^{-2} sr^{-1}). The heavy contours, adapted from Dubner and Arnal (1988), indicate CO emission from the east cloud (depicted as antenna temperatures, linearly, from 1 to 5 K km^{-1} s^{-1}). The 6′ diameter regions observed by Szymkowiak (1985) using the *Einstein Observatory*'s solid state spectrometer (SSS) are indicated.

the east cloud assuming that the dust in this neutral and molecular cloud (Dubner and Arnal 1988) is heated by the ISRF. Radiative heating of the dust by the emission of the SNR was neglected, since the relevant optical and UV integrated fluxes are not well-known. Furthermore, the total optical emission is unlikely to be able to significantly heat the bulk of the cloud (which is $\sim 20'$ or ~ 12 pc from the SNR), and we see no obvious signs of heating in the portion of the cloud nearest the remnant when compared to portions farther away.

Next we modeled regions inside the remnant whose gas densities and temperatures are constrained from X-ray studies. The most suitable regions were those observed with the solid state spectrometer (SSS) of the *Einstein Observatory* (Giacconi *et al.* 1979) and analyzed by Szymkowiak (1985). The *Einstein Observatory* obtained SSS spectra of Puppis A at eight regions across the SNR. The locations and designations of these regions are indicated in Figure 1. The regions are 6′ in diameter (corresponding to 3.5 pc at a 2 kpc distance), which is a good match to the resolution of the IR data (see § II). Szymkowiak (1985) combined the data from regions with similar spectra, resulting in four distinct spectra (designated C, R, I, and N) which he fit with nonequilibrium ionization (NIE) models. Each NIE model is characterized by whether or not the electron and ion temperatures have equilibrated behind the shock ($T_e = T_i$ or $T_e \neq T_i$). The models yield two sets of shock temperature (T_s) and collisional time scale parameter ($\eta \equiv n_0^2 E$, where n_0 is the ambient density and E is the explosion energy) which provided the best fits to the data. In Table 4 we list the X-ray derived gas properties applicable to the various regions. For sake of simplicity, we took the gas temperature in the regions to be equal to the shock temperature T_s, even though the relevant temperature is that of the electrons which may (or may not) be equilibrated with that of the ions (Itoh 1978; Hamilton, Sarazin, and Chevalier 1983). Furthermore, we took the electron density to be equal to $4n_o = 4[\eta/E]^{1/2}$, and the explosion energy E to be equal to 10^{51} ergs. The best gas parameters for X-ray spectra of regions I1, I2, I3, and N are not unique (and depend on whether the electron-ion temperature equilibrated behind the shock). An important goal of this paper is to examine to what extent the IR observations of these select regions can resolve the ambiguity in their gas parameters.

The modeling of the spectrum from region C was of particular interest since this region, which contains the eastern knot, is the portion of the remnant most directly associated with the east cloud. Dust giving rise to the IR emission from this region is probably shock-processed dust from the east cloud. Thus, by comparing the dust in the east cloud with that in region C, we can gain excellent "before-and-after" pictures of dust as it passes through a strong shock.

We also modeled the integrated IR emission of the entire SNR. As indicated by analysis of both *Einstein* and *EXOSAT* results (Szymkowiak 1985; Petre *et al.* 1982; Aschenbach 1985), there is no single temperature or density which applies to the entire SNR. The temperature, density, and grain size distribution required to fit the integrated spectrum of Puppis A might not be those of any particular region within the SNR. In this case, the physical model will serve as a guide to the differences that can arise when one can only study the integrated emission of an inhomogeneous source.

TABLE 4

PARAMETERS OF BEST X-RAY MODELS (FROM SZYMKOWIAK 1985)

Model Designation	Regions Modeled	log T_s (K)	log η (ergs cm^{-6})	n_e (cm^{-3})
C	C	6.50	51	4.0
R	R1+R2+R3	6.50	50	1.3
I	I1+I2+I3	6.75	50	1.3
N	N	7.00	50	1.3
NI	N, I1+I2+I3	7.00	49	0.4

The relative sizes of the uncertainties in the flux densities are smaller for most of the SSS regions than for the whole remnant because the regions are small and (generally) have higher average surface brightnesses. As demonstrated below, this allows us to make finer distinctions in the modeling of the 6′ SSS regions than the 56′ remnant. The results of the physical modelling are presented in Tables 5 and 6, with some specific description of the individual cases given below.

a) The East Cloud: Enhancement of Small Grains

The east cloud was modeled under the assumption that the dust is heated only by the ISRF as specified by Mathis, Mezger, and Panagia (1978). Grains at their equilibrium temperatures can reproduce the observed 60 and 100 μm emission of the east cloud, but the observed emission at 12 and 25 μm can only be modeled by small grains ($a < 100$ Å) with their fluctuating (and occasionally quite high) temperatures. Using the eMRN grain size distribution (§ IV), we find that the predicted emission at 12 and 25 μm is too low by factors of ~ 20 and ~ 2, respectively. Including a break in the grain size distribution for graphite grains at 30 Å to a steeper power law ($k = -5.0$) at small sizes (similar to results found by Draine and Anderson 1985) improves the fit at 25 μm, but is still low at 12 μm by a factor of ~ 5. For this eMRN + VSG distribution over one-third of the graphite (by mass) is in the abundant small grains. We also tried to apply an eMRN distribution with an additional component of small graphite grains (3–10 Å) with a steep spectrum ($k = -5.0$), as proposed by Weiland *et al.* (1986). Here the size spectrum of the very small grains was not constrained to merge continuously into the eMRN size distribution. This gives a slightly better fit than the eMRN + VSG distribution, though it is still low by a factor of 2 at 12 μm. This distribution assumes that about 40% of the dust mass is in the eMRN component, and the remaining 60% resides in the additional small grain component.

Figure 2 shows the resultant spectra from ISRF heating of MRN grain size distributions with lower limits of 100 Å (*dotted line*), and 3 Å (*dashed line*), and from the eMRN + VSG distribution (*solid line*).

b) Region C: Sputtering of Dust Grains

This region, containing the eastern knot, is the brightest portion of the remnant in the IR, and is the only place at which 12 μm emission is detected (see Fig. 3). The emission at 12 μm is very sensitive to the abundance of small dust grains and the amount of sputtering. Thus, for this region we have the best 12 μm constraint on sputtering, in addition to the constraints which arise from the relatively small errors on the 25 and 60 μm flux densities. Region C is also immediately adjacent to the east cloud. This proximity to the east cloud means that our initially measured flux densities were probably contaminated by emission from the east cloud. Therefore, we assumed that the east cloud contributed emission across the area of region C at the same brightness as is observed in the immediately adjoining area exterior to the remnant. Each band was adjusted

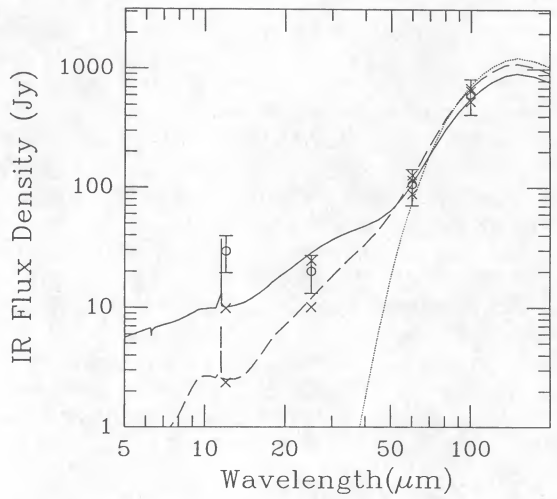

FIG. 2.—Model spectra of the east cloud. Observed data are represented by open circles with error bars. Model spectra are indicated by the lines. Crosses (×) denote the model spectra convolved with the *IRAS* spectral response in each band. These should be compared to the observed data points. Large grains ($a > 100$ Å) are essentially at their equilibrium temperatures, and cannot reproduce the observed 12 and 25 μm emission (*dotted line*). Extending the MRN distribution to grains as small as 3 Å (eMRN distribution, see text) gives a better fit, but still underestimates the 12 μm emission (*dashed line*). Including an additional enhancement of small grains (eMRN + VSG distribution, see text) enables the best fit to the data (*solid line*).

independently, and the estimated errors of the flux densities were increased to reflect the uncertainties in the amount of emission contributed by the east cloud. These changes were most significant at 12 and 100 μm. Recently, it has become apparent that interaction with the east cloud is the cause of the enhanced X-ray, IR and optical brightness of the SNR in the area of Region C. Petre *et al.* (1982) and Dubner and Arnal (1988) present X-ray and radio observations indicating that the eastern knot is material from the east cloud which has been swept up into the remnant. (The case for this interaction from these observations and the IR data has been discussed in Paper I.) Therefore, we have assumed that the grains of Region C followed the same eMRN + VSG size distribution as the east cloud when they were initially engulfed by the SNR.

With this enhanced population of small grains, and the plasma conditions given by Szymkowiak (1985), we find the dust emits too strongly at 12 and 25 μm to fit the observed emission (see Fig. 4). Amounts of sputtering between ~5 and ~25 Å give rise to spectra with the right slope between 25 and 60 μm, and which fit the observed 12 μm emission. The best fit, occurring with $\Delta a = 18$ Å of sputtering, is also illustrated in Figure 4. The model described above is, however, not unique. An equally good fit to the data can be achieved with an eMRN grain size distribution (without any initial VSG component) and less sputtering ($\Delta a = 15$ Å).

c) *Regions I1, I2, I3, and N: Plasma Conditions*

Szymkowiak (1985) found two different sets of T_s and η which could be used to model the X-ray spectra of these regions. For regions I1, I2, and I3 he found that the conditions of model I ($T_s = 5.6 \times 10^6$ K, $\eta = 10^{50}$ ergs cm^{-6}) provided a better fit than the conditions of model NI ($T_s = 10^7$ K, $\eta = 10^{49}$ ergs cm^{-6}) to the combined X-ray emission of these regions. Our models of the IR emission using each of these sets of plasma conditions supports Szymkowiak's (1985) finding. The conditions of model I can provide a good fit to the observed IR flux densities using the eMRN grain size distribution subjected to ~2–3 Å of sputtering. For the same grain size distribution conditions of model NI lead to IR spectra which are too steep in the 25–60 μm range to fit the observations, even when no sputtering is considered. The comparison of these two sets of plasma conditions is shown in Figure 5. There is a slight improvement of the fit from Region I1 to I2 to I3, but there are no definite implications for systematic variations of

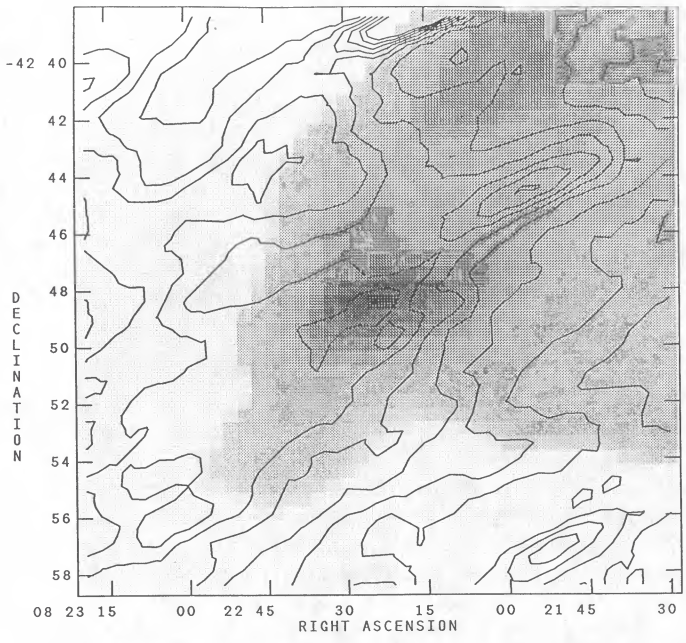

FIG. 3.—This logarithmic gray-scale map depicts a close-up of the region surrounding the eastern knot at 25 μm. The contours of 0, 2, 4, 6, 8, 10, 12, 14, 16, and 18×10^{-8} W m^{-2} sr^{-1} indicate the 12 μm emission in this area. Notice that there is a weak, but distinct, peak in the 12 μm emission at the location of the eastern knot ($\alpha = 8^h22^m25^s$, $\delta = -42°48'.5$).

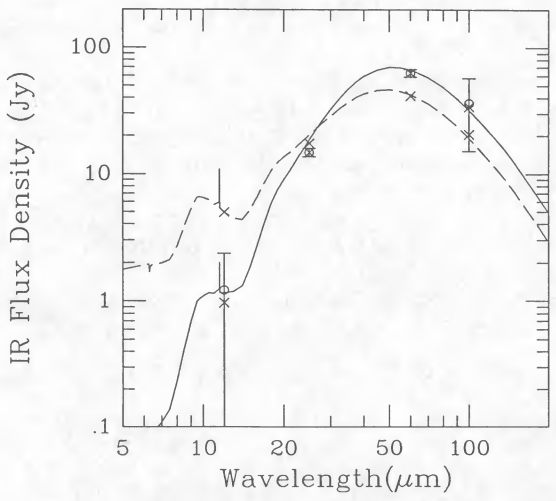

FIG. 4.—Model spectra of region C. The symbols are as in Fig. 2. These spectra are fit to the observed data after emission from the east cloud has been subtracted. The dashed line is the spectrum produced by the eMRN + VSG grain size distribution without any sputtering. It is clearly not steep enough between 12 and 60 μm to fit the observations. If the size distribution has been sputtered by 18 Å, the spectrum steepens and a good fit is obtained (*solid line*).

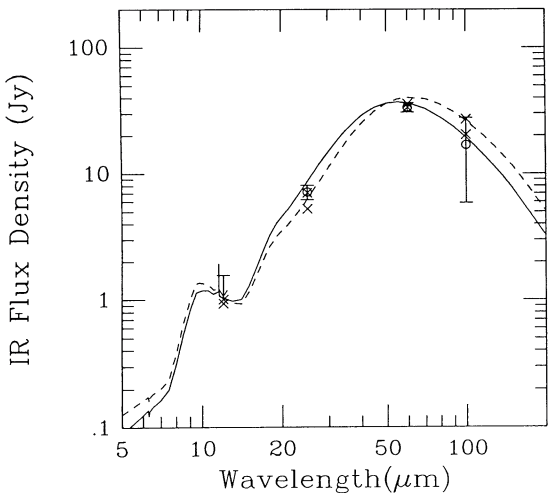

FIG. 5.—Model spectra for region I3. The symbols are as in Fig. 2, except at 12 μm the observed upper limit is indicated by the downward arrow. The solid line shows the spectrum modeled from the plasma parameters of model I with 3 Å of sputtering (derived results listed in Table 5). The dashed line indicates the spectrum from model NI with no sputtering.

the temperature, density, or amount of sputtering. The improvement could be due to less contamination of the measured flux densities with increasing distance from the east cloud.

For region N, Szymkowiak (1985) found that the conditions of models *N* ($T_s = 10^7$ K, $\eta = 10^{50}$ ergs cm^{-6}) and NI ($T_s = 10^7$ K, $\eta = 10^{49}$ ergs cm^{-6}) led to equally good models of the X-ray spectrum. Applying these conditions to modeling the IR data, we find that the conditions of model N are the most appropriate. The best fit results if we assume the eMRN distribution has been subjected to 4 Å of sputtering. The conditions of model NI produce IR spectra which are too steep between 25 and 60 μm even if no sputtering is included (see Fig. 6). If we apply a grain size distribution with enhanced abundances of small grains (as found for the east cloud), the fit for the conditions of model NI can be improved, but a better fit is still found using model N.

d) Region R3: Possible Large Grains

Region R3 is located in the "hook" of Puppis A. This region differs from the rest of Puppis A in that its IR emission is very weak relative to its radio emission (Paper I). Like region C it is also located near the east cloud, and may also be a result of the interaction between the cloud and remnant. (While regions R1 and R2 show X-ray spectra similar to, though weaker than, that of region R3, their IR intensities are too low for any meaningful analysis.)

Models of the IR emission are not tightly constrained because of the relatively large uncertainties in the flux densities (due to fainter emission at this location). The best fit for the eMRN size distribution is with $\Delta a_{\rm sput} = 4$ Å, although with sputtering between 0 and $\sim$35 Å, either the eMRN or the eMRN + VSG grain size distributions can fit the observations, except at 100 μm. If the 25 and 60 μm flux data are fit well, then the modeled IR emission at 100 μm is lower than the observed emission by more than the estimated 3 σ error. This difference can be reduced if there are more large grains in this region than elsewhere within the SNR. Changing the upper limit of the eMRN grain size distribution from 0.25 μm to 1.0 μm, adds enough large grains to bring the 100 μm flux density within the 3 σ error. This change is illustrated in Figure 7. Note that the additional large grains do not affect the fit at 12 or 25 μm significantly. However, we have no other evidence from other regions of the remnant or from the east cloud, that large grains might be present in the vicinity of Puppis A. It is only the peculiar (and unexplained) relative radio, IR, and X-ray brightnesses of this portion of the remnant (Paper I), which allow us to speculate that there may be peculiarities in the dust as well.

Lying near the east cloud, it is also possible that much of the problem in fitting the 100 μm flux density of region R3 is due to contamination by emission from the cloud, as we assumed for region C. If this is the case, models of the IR emission without

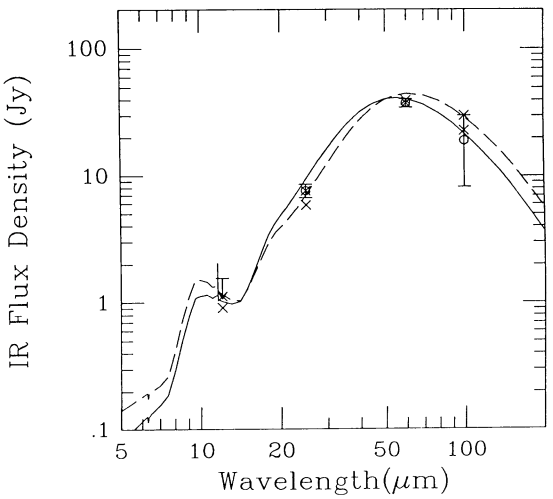

FIG. 6.—Model spectra for region N. The symbols are as in Fig. 2, except at 12 μm the observed upper limit is indicated by the downward arrow. The solid line shows the spectrum modeled from the plasma parameters of model N with 4 Å of sputtering (derived results listed in Table 5). The dashed line indicates the spectrum from model NI with no sputtering.

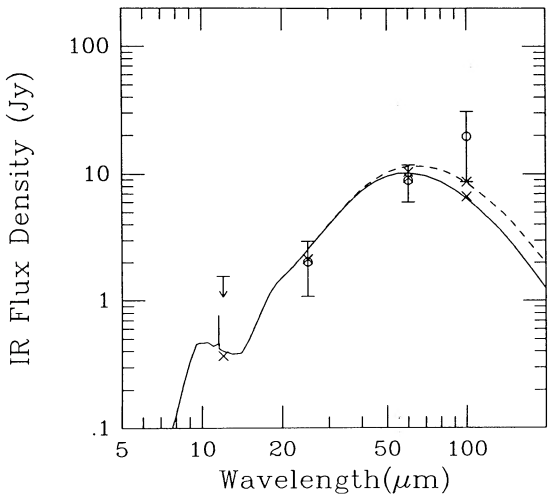

FIG. 7.—Model spectra for region R3. The symbols are as in Fig. 2, except at 12 μm the observed upper limit is indicated by the downward arrow. The solid line indicates the spectrum from the eMRN grain size distribution with 4 Å of sputtering (derived results listed in Table 5). The dashed line shows the spectrum modeled from the eMRN size distribution extended to include grains up to 1.0 μm, also with 4 Å of sputtering. This latter spectrum has been normalized to match the eMRN spectrum at the shorter wavelengths.

the additional large grains can reproduce the observed spectrum fairly well. Conversely, if the cloud does not actually extend slightly in front of or behind the remnant, then the fits for region C can be improved with the assumption of additional large grains.

e) *Total SNR: Global Average*

The total IR emission of the SNR can also be modeled in the same manner as the individual regions. In this case, no definite temperature and density can be assigned to the remnant in advance. However, since there are no dramatic spectral differences across the SNR, and since the SSS observed regions account for almost 20% of the total emission, we constrained the models by the temperature-density combinations found by Szymkowiak (1985). We also used the eMRN grain size distribution, which seems to be an acceptable initial distribution for the entire remnant. With no sputtering, all of the plasma conditions led to models which fit within the errors, but the best fit to the total emission came from the conditions of model I ($T_s = 5.6 \times 10^6$ K, $\eta = 10^{50}$ ergs cm^{-6}). Figure 8*a* illustrates the best and extreme models with no sputtering included. For the conditions of model I, sputtering by ~ 2 Å improves the fit slightly, although it takes ~ 30 Å of sputtering before the model cannot fit within the errors (see Fig. 8*b*). The best fit allowing sputtering is from the conditions of model R ($T_s = 3.2 \times 10^6$ K, $\eta = 10^{50}$ ergs cm^{-6}) with 5 Å of sputtering (see Fig. 8*b*). The conditions of model C ($T_s = 3.2 \times 10^6$ K, $\eta = 10^{51}$ ergs cm^{-6}) can provide a fit almost as good if the sputtering is assumed to be ~ 18 Å.

VI. DISCUSSION

In the analysis of Puppis A we made two important assumptions: that the distance to the remnant is 2.0 kpc, and that the remnant is spherically symmetric. The adopted distance of 2.0 kpc is close to the kinematic distance (2.2 kpc, Dubner and Arnal 1988) and $\Sigma - D$ distances (2.4 kpc, Caswell and Lerche 1979; 1.8 kpc, Milne 1979). Optical observations of the motions of filaments within Puppis A (Winkler *et al.* 1988) are also consistent with a distance of 2 kpc. The only derived quantities that are directly affected by this first assumption are the infrared luminosity and mass of the swept-up gas and dust.

The assumption of spherical geometry, and hence the concept of remnant radius, are clearly a simplification of the actual appearance of the remnant. However, the location of the expansion center determined by the motions of optical filaments (Winkler *et al.* 1988) is near the center of the observed infrared emission. Therefore, the best estimate of the radius for our purposes is the average extent of emission outward from the center of the remnant, which is $\sim 28'$. At a distance of 2.0 kpc this corresponds to 16.3 pc. The quantities most affected by this second assumption are those derived from the Sedov solution, including the age of the remnant, the energy of the explosion, and the average density of the ambient ISM.

In the following sections, we discuss the results of our paper, and describe their sensitivity to the assumptions.

a) *Evidence for Grain Processing*

To make any inferences on grain processing inside the remnant, we must assume that we have a reasonable knowledge of the grain size distribution ahead of the shock. *IRAS* observations of a variety of astrophysical environments, including diffuse clouds (e.g. Weiland *et al.* 1986) and reflection nebulae (Luan *et al.* 1989), suggest that the grain size distribution in the diffuse ISM can be characterized by an eMRN+VSG distribution. Conservatively, we adopted an eMRN distribution in most of our models except for region C, since the material from this region probably originated from the east cloud, which is best modeled by an eMRN+VSG distribution. The results show that in order to fit the IR emission from the remnant, the initial grain sizes have to be sputtered by amounts of 5–30 Å, depending on the assumed density and gas temperature of the remnant. Of course, the amount of sputtering is dependent upon the assumed initial abundance of small grains. The strongest evidence for grain processing is provided by the IR emission from region C which is immediately adjacent to the east cloud. An initial eMRN+VSG

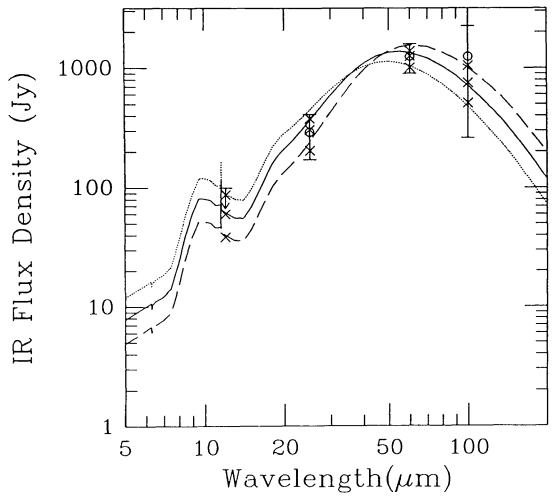

FIG. 8*a*

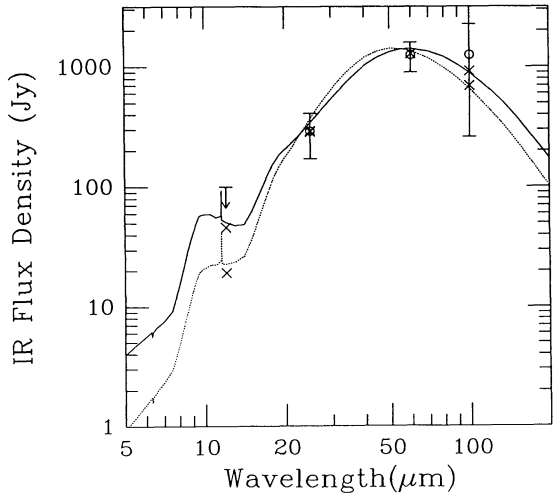

FIG. 8*b*

FIG. 8.—Model spectra for the total emission of Puppis A. The symbols are as in Fig. 2, except at 12 μm the observed upper limit is indicated by the downward arrow. (*a*) All spectra are calculated using the eMRN distribution with no sputtering. The best fit was calculated using $T_6 = 5.6$ (10^6 K), $n = 1.3$ cm^{-3} (conditions I, *solid line*). The dotted and dashed lines represent the extreme fits calculated from the conditions of models C and N, respectively. (*b*) The solid line shows the spectrum of the eMRN distribution after 5 Å of sputtering for the conditions of model R. This is the best fit of any model to these data. Another good fit is provided by the eMRN distribution after 18 Å of sputtering for conditions of model C (*dashed line*).

TABLE 5

DETAILED MODELING OF THE EAST CLOUD AND REGIONS OF PUPPIS A

Region:	East Cloud	C	I1	I2	I3	N	R3
OBSERVATIONS							
IRAS Flux Densities (Jy)[a] 12 μm	29.6	1.22	<1.56	<1.56	<1.56	<1.56	<1.56
25 μm	20.3	14.8	13.1	10.2	7.2	7.7	2.0
60 μm	107.	63.2	50.7	44.7	33.7	37.9	8.9
100 μm	619.	36.3	44.6	31.7	16.9	19.2	19.7
MODEL INPUT PARAMETERS							
Gas Density (cm^{-3})[b]	...	4.0	1.3	1.3	1.3	1.3	1.3
Gas Temperature (10^6 K)[b]	...	3.2	5.6	5.6	5.6	10.	3.2
Grain Size Distribution[c]	eMRN + VSG	eMRN + VSG	eMRN	eMRN	eMRN	eMRN	eMRN
Δa_{sput} (Å)	0	18	3	2	3	2	4
MODEL SPECTRA							
Model Flux Densities (Jy) 12 μm	9.91	0.97	1.51	1.47	0.94	0.77	0.37
25 μm	24.8	14.8	11.5	9.98	7.11	7.75	2.13
60 μm	115.	63.2	54.4	45.3	33.7	37.7	9.31
100 μm	538.	34.2	33.0	27.4	20.4	20.0	6.65
DERIVED PARAMETERS							
Sputtering Age, τ (yr)	0	900	450	300	450	300	600
Radiating Dust Mass (10^{-3} $M_\odot$)[d]	23500	6.56	7.96	6.64	4.92	3.54	2.40
Dust Depletion, δ	1.0	0.69	0.93	0.95	0.93	0.95	0.91
Shocked Gas Mass ($M_\odot$)[d]	3140	1.23	1.11	0.908	0.687	0.484	0.343
Effective Thickness of Emitting Region (pc)	...	1.0	2.8	2.3	1.7	1.2	0.86
IR Luminosity ($L_\odot$)[d]	4080	668	588	504	363	394	107

[a] Errors for the east cloud were taken to be 33% in all bands. Errors for the SSS regions are 0.77, 0.94, 3.9, and 11 Jy at 12, 25, 60, and 100 μm.
[b] From Szymkowiak 1985.
[c] eMRN → $n_i(a) \sim a^{-3.5}$, 3 Å < a < 0.25 μm;
eMRN + VSG → $n_i(a) \sim a^{-5.0}$, 3 Å < a < 30 Å; $n_i(a) \sim a^{-3.5}$, 30 Å < a < 0.25 μm (graphite grains);
$n_i(a) \sim a^{-3.5}$, 3 Å < a < 0.25 μm (silicate grains).
[d] Normalized to a distance of 2 kpc.

grain size distribution has to be sputtered by an amount of $\Delta a \approx 18$ Å to reproduce the observed IR spectra. We note that even *without* the VSG component, sputtering is still required to produce the best fitting spectrum. In this case the amount of sputtering is slightly less ($\Delta a \approx 15$ Å).

Sputtering will destroy the smallest grains while leaving the largest grains essentially unchanged, and will noticeably alter the IR spectrum at the shorter wavelengths, even when the mass depletion of the dust is as small as 10%. The depletion factors found in the physical models generally indicate that $\lesssim 10\%$ of the dust (by mass) has been sputtered away and returned to the gas phase (see Tables 5 and 6). At the location of region C, as much as 30% of the dust mass has been destroyed.

b) *Dust Temperature*

The most basic quantity we derived from our analysis is the dust color temperature as determined from the 2 to 3, and 3 to 4 band ratios. We found that the IR emission, integrated across the entire SNR, has color temperatures of $T_{23} = 65$ K and $T_{34} = 44$ K. There were no indications that these color temperatures varied across the remnant on scales of $\gtrsim 7'$, but the uncertainties involved (especially for T_{34}) could obscure actual variations which may be present.

In the course of the physical analysis, we calculated $T_{eq}(a)$, the physical (equilibrium) temperatures of grains of various sizes a. The 60–100 μm color temperature derived from these physical models, which give the best fit to the observed 25–100 μm fluxes, is generally much higher than the observed global value of 44 K. The fact that these models provide the best fit to the data underscores the large uncertainties in the 100 μm fluxes. The equilibrium dust temperature of 0.1 μm dust particles is about 44 K, in reasonable agreement with the observed value of T_{34}. This suggests that the results derived in our generic dust calculations, where we attributed the IR emission to a population of 0.1 μm sized dust particles radiating at $T_{eq} = 44$ K, should be not far off those derived in the physical models. The 25–60 μm color temperature (T_{23}) is generally higher than T_{34}, reflecting the presence of a range of grain temperatures, and the effect of stochastically heated dust particles on the short-wavelength emission.

TABLE 6

PHYSICAL MODELING OF THE TOTAL EMISSION OF PUPPIS A

		I	R
MODEL INPUT PARAMETERS			
Plasma Model		I	R
Gas Density (cm^{-3})		1.3	1.3
Gas Temperature (10^6 K)		5.6	3.2
Grain Size Distribution[a]		eMRN	eMRN
Δa_{sput} (Å)		0	5
MODEL SPECTRA			
Model Flux Densities (Jy)	12 μm	60.2	46.4
	25 μm	306.	287.
	60 μm	1260	1290
	100 μm	752.	922.
DERIVED PARAMETERS			
Sputtering Age, τ (yr)		0	770
Radiating Dust Mass ($M_\odot$)[b]		0.19	0.34
Dust Depletion, δ		1.0	0.89
Shocked Gas Mass ($M_\odot$)[b]		25.	50.
Effective Thickness (pc)		0.73	1.5
IR Luminosity ($L_\odot$)[b]		15000	14000

[a] eMRN → $n_i(a) \sim a^{-3.5}$, 3 Å < a < 0.25 μm
[b] Normalized to a distance of 2 kpc.

c) Infrared Luminosity, Dust and Gas Masses

In both the generic dust and physical analyses of the integrated emission from Puppis A, the infrared luminosity is about 14,000 $L_\odot$. The luminosity is nearly independent of the details of the modeling (other than the assumed distance) since it is directly proportional to the observed IR flux. The IR luminosity exceeds that in the X-ray regime by a factor of ~ 8, indicating that gas-grain collisions are the major gas cooling mechanism of the shocked ISM (Dwek *et al.* 1987). The generic dust models (§ III) estimate a dust mass is in the range of 0.16–0.43 $M_\odot$, where this range is determined by our variations in the dust temperature. The physical models (§ V*e*) indicate a total mass of the remnant in the narrower range of 0.19–0.34 $M_\odot$. Here the range stems from our uncertainty in the plasma conditions. Of course, in both analyses the derived dust mass also depends on the assumed distance to Puppis A. In spite of the uncertainties, the dust masses derived from the generic dust and physical analyses are very similar, indicating the consistency of the assumptions made in the generic dust analysis. From the dust mass we can derive that of the gas by adopting a gas-to-dust mass ratio. For a ratio of 0.0077, the total mass of gas within Puppis A is between 21 and 56 $M_\odot$.

d) Remnant Density, Temperature, and Structure

The IR emission from collisionally heated dust particles can be used to constrain the physical conditions of the shocked gas. At gas temperatures above $\sim 10^7$ K, the IR spectrum is mainly sensitive to the density of the shocked gas, which can therefore be directly determined from the IR observations. Below temperatures of $\sim 10^7$ K, as in the case of Puppis A, the IR observations can only constrain the various gas temperature-density combinations that can produce the observed spectrum. It was therefore of interest to see if the gas parameters derived by Szymkowiak (1985) would be able to produce the observed IR flux, or, where the gas parameters were not uniquely determined by the X-ray observations, if the IR observations could favor one set of parameters over the other. It is important to point out that any comparison between IR and X-ray observations cannot prove the correctness (or uniqueness) of a given model, just its consistency. On the other hand, such comparison can be used to definitely rule out sets of gas parameters which cannot reproduce both, the IR and X-ray spectra of the emitting region.

We were successfully able to model the IR emission of the regions studied by Szymkowiak (1985) by using the local plasma temperatures and densities which he derived from the X-ray spectra. In fact, for region N, we were able to discriminate between different sets of temperature and density, which yielded equally good fits to the X-ray spectra, by showing that one set produced a better IR spectrum (§ V*c*).

The physical models of the SSS regions indicate that densities of the X-ray emitting plasma ranges over at least ~ 1–4 cm^{-3}, and temperatures range at least over ~ 3–10×10^6 K. The highest density region (region C) possesses the lowest temperature, while lower density regions span the range of temperatures. The best physical models of the integrated emission indicate that a density of ~ 1.3 cm^{-3} and a temperature of 3–6×10^6 K are appropriate averages for the IR emitting regions of the remnant. The implied ISM density is ~ 0.3 cm^{-3}. This figure is higher than the mean ISM density of $\lesssim 0.1$ cm^{-3} calculated using the generic dust model of § III. The lower density found in the generic dust model leads to the correspondingly higher gas temperature.

The densities calculated by different techniques give us hints as to the original distribution of material in the vicinity of Puppis A. The globally determined density $n_0 \lesssim 0.1$ cm^{-3} (from § III) gives the mean density of all the material swept up by the SNR. The density of $n_0 \approx 0.3$ cm^{-3}, which is compatible with the physical modelling of the integrated emission of Puppis A, indicates that most of the material was initially found in regions ~ 3 times denser than the average ISM density. This distribution of this denser material may have been clumps which were initially uniformly scattered throughout the region. Another possibility is that the expanding SNR has encountered denser than average material only recently. This possibility has the appeal that it would naturally explain why most regions of the SNR show relatively little sputtering. The dense material could be part of existing structures, i.e., the outer portions of the east cloud and the ridge, or it could have been in a structure which is no longer visible, such as a cavity which Puppis A has now filled or overfilled. The lack of large amounts of grain destruction indicates that most of the mass could not have been swept up when the SNR was very young.

The structure of the SNR itself is revealed through its density variations, morphology and line of sight thickness. The effective thicknesses of ~ 2–3 pc for regions I1–I3 are in fair agreement with Szymkowiak's (1985) estimate of ~ 3 pc thickness. If we are seeing emission from both sides of a shell of emitting material, the thickness of the shell, ~ 1–2 pc, is roughly 10% of the shell radius. With a shell-like geometry, we would expect regions near the edge to have higher effective thicknesses than regions near the center of the SNR. Contrary to these expectations, the higher density and lower thickness of Region C probably reflect that most of the emission here is from the small bright knot rather than the long line of sight offered through the edge of a uniform shell. A shell only 1–2 pc thick would appear with an angular thickness of ~ 2–3′. Therefore, with the *IRAS* data there would be little hope of resolving differences between the inner and outer edges of such a shell even if the geometry of the SNR were simpler than appears to be the case for Puppis A. Regardless of the actual distribution of material, the low effective thickness derived from the integrated emission (Table 6) indicates that the volume-filling factor of the IR emitting regions is less than 10%.

e) Remnant Age and Explosion Energy

The evidence for grain processing discussed above is extremely important, since, if attributed to thermal sputtering, it can yield information on the amount of time the dust particles have been eroded by the ambient gas, that is, the time since the given parcel of gas was swept up by the expanding SN blast wave. Region C is the site of recent interaction with the east cloud, and should contain dust which has been subjected to sputtering for only a relatively short time. Other regions (N and I3 in particular) include longer lines of sight through the interior of the remnant and might be expected to contain dust which has been subjected to sputtering a large fraction of the age of the remnant. Since the sputtering ages for regions I3 and N are shorter than for region C, the IR emission must arise only from relatively recently swept-up dust in the shell and not from older dust in the interior portions of the SNR. Region C would still appear to be slightly older than other regions, even if we were to assume an initial enhancement of small grains across the entire remnant, rather than only at region C. This maximum sputtering age of ~ 900 yr places a lower limit to the age of Puppis A. This lower limit is consistent with recent estimates of 2000–5000 yr, (Milne *et al.* 1983), based on the

radio surface brightness and polarization characteristics, or of 3700 ± 300 yr (Winkler *et al.* 1988), based on the proper motions of optical filaments. The 6000 yr age derived here by application of the Sedov solution in the generic dust model (§ III), is significantly longer than these estimates. However, we point out that this result is very sensitive to small changes in the adopted dust temperature.

The initial kinetic energy of the explosion calculated using the generic dust model ranges from 0.3×10^{51} to 1×10^{51} ergs. This figure is quite sensitive to both the assumed distance and dust temperature, and also assumes that the Sedov solution applies to Puppis A at the present epoch. For the physical models (§ V), an initial kinetic energy had to be assumed. We adopted the canonical 10^{51} ergs, which yielded values for physical parameters that were generally consistent with the generic dust analysis and other estimates.

VII. SUMMARY

In this work we have used two methods to analyze the IR emission from the remnant and its surrounding medium. In the first method we did not concern ourselves with details of the dust properties or the heating mechanism. The advantage of this approach is that it is applied without the need for constraints derived from X-ray observations, and that it yields global parameters of the SNR and the surrounding medium. The second method uses a physical approach to modeling the IR emission. In this method we employ the results of previous X-ray analysis to calculate the details of the dust heating mechanism, thereby deriving the grain size distribution, the dust mass, and the amount of grain destruction, as well as remnant and ISM parameters.

Using the first modeling approach, we derived the following results: (*a*) the average dust color temperatures are $T_{34} = 44$ K, and $T_{23} = 65$ K; (*b*) the IR luminosity and dust mass (assuming a source distance of 2 kpc) are 14,000 $L_\odot$ and 0.25 $M_\odot$, respectively. The IR luminosity exceeds that in the X-rays by about a factor of 8. Adopting a dust-to-gas mass ratio of 0.0077, we derive a gas mass of 33 $M_\odot$; (*c*) assuming that the remnant is spherically symmetric with an angular radius of 28′, we derive an ISM gas density of ~ 0.06 cm^{-3}, and a postshock density of ~ 0.24 cm^{-3}. Combined with the dust temperature (44 K) and the fact that the dust is collisionally heated, we derive a postshock gas temperature of $\sim 1.5 \times 10^7$ K; (*d*) applying the Sedov solution to the remnant, we derive an age and explosion energy of 6,000 yr, and 0.6×10^{51} ergs respectively, for the remnant.

Using a detailed physical model to describe the interaction between the gas and dust in the postshock region we derived the following results: (*a*) the MRN dust model needs to be extended to very small grain sizes in order to model the observed 25 and 60 μm emission from the remnant; (*b*) there is evidence for grain processing behind the shock. Comparing the initial grain size distribution (as derived from the IR emission of the eastern cloud which is being swept up by the remnant) with that required to model the IR emission from region C (the segment of the eastern cloud overrun by the shock) we find a decrease of 30% in the dust mass, and infer a sputtering time of 900 yr; (*c*) modeling the IR emission from localized regions inside the remnant shows that the X-ray derived gas densities and temperatures are consistent with those required to account for the observed infrared spectrum; (*d*) modeling the integrated IR fluxes gives average gas densities and temperatures of 1.3 cm^{-3} and 3.2×10^6 K, respectively; (*e*) IR luminosities and dust masses are 14,000 $L_\odot$ and 0.34 $M_\odot$, respectively. The gas mass (assuming an initial dust-to-gas mass ratio of 0.0077) is 50 $M_\odot$; (*f*) The average depletion factor (by mass) of the dust is 0.89, yielding a sputtering age of 770 yr; (*g*) The average thickness of the IR emitting region is ~ 1 pc, about 10% of the average radius of the remnant.

J. Dickel has provided helpful discussion on aspects of this work. Much of the work presented here was used in a preliminary form by R. G. A. as part of a Ph.D. dissertation at the University of Illinois. R. G. A. has been supported under the NASA Graduate Student Researchers Program (Grant NGT-50152), and NASA contract JPL958014.

REFERENCES

Arendt, R. G. 1989, *Ap. J. Suppl.*, **70**, 181.
Arendt, R. G., Dwek, E., Petre, R., Dickel, J. R., Roger, R. S., Milne, D. K., and Kesteven, M. J. 1990, *Ap. J.*, **350**, 266 (Paper I).
Aschenbach, B. 1985, *Space Sci. Rev.*, **40**, 447.
Cameron, A. G. W. 1982, in *Essays in Nuclear Astrophysics*, ed. C. A. Barnes, D. D. Clayton, and D. N. Schramm (Cambridge: Cambridge University Press), p. 23.
Casoli, F., Dupraz, C., Gerin, M., Combes, F., and Boulanger, F. 1986, *Astr. Ap.*, **169**, 281.
Caswell, J. L., and Lerche, I. 1979, *M.N.R.A.S.*, **187**, 201.
Draine, B. T. 1987, *Princeton Observatory Preprints*, No. 213.
Draine, B. T., and Anderson, N. 1985, *Ap. J.*, **292**, 494.
Draine, B. T., and Lee, H. M. 1984, *Ap. J.*, **285**, 89.
Draine, B. T., and Salpeter, E. E. 1979, *Ap. J.*, **231**, 77.
Dubner, G. M., and Arnal, E. M. 1988, *Astr. Ap. Suppl.*, **75**, 363.
Dwek, E. 1986, *Ap. J.*, **302**, 363.
———. 1987, *Ap. J.*, **322**, 812.
Dwek, E., Petre, R., Szymkowiak, A., and Rice, W. L. 1987, *Ap. J. (Letters)*, **320**, L27.
Elliott, K. H., Goudis, C., and Meaburn, J. 1976, *M.N.R.A.S.*, **175**, 605.
Giacconi, R., *et al.* 1979, *Ap. J.*, **230**, 540.
Hamilton, A. J. S., Sarazin, C. L., and Chevalier, R. A. 1983, *Ap. J. Suppl.*, **51**, 115.
Herbst, W. 1975, *A.J.*, **80**, 212.
IRAS Catalogs and Atlases; Explanatory Supplement 1985, ed. C. A. Beichman, G. Neugebauer, H. J. Habing, P. E. Clegg, and T. J. Chester (Washington, DC: GPO).
Itoh, H. 1978, *Publ. Astr. Soc. Japan*, **30**, 489.
Low, F. J., *et al.* 1984, *Ap. J. (Letters)*, **278**, L19.
Luan, L., Werner, M. W., Dwek, E., and Sellgren, K. 1989, in *Interstellar Dust: Contributed Papers*, ed. A. G. G. M. Tielens and L. J. Allamandola, (NASA CR 3036), p. 135.
Mathis, J. S., Mezger, P. G., and Panagia, N. 1978, *Astr. Ap.*, **128**, 212.
Mathis, J. S., Rumpl, W., and Nordsieck, K. H. 1977, *Ap. J.*, **217**, 425 (MRN).
Milne, D. K. 1971, *Australian J. Phys.*, **24**, 429.
———. 1979, *Australian J. Phys.*, **32**, 83.
Milne, D. K., Goss, W. M., and Danziger, I. J. 1983, *M.N.R.A.S.*, **204**, 237.
Neugebauer, G. *et al.* 1984, *Ap. J. (Letters)*, **278**, L1.
Petre, R., Canizares, C. R., Kriss, G. A., and Winkler, P. F. 1982, *Ap. J.*, **258**, 22.
Szymkowiak, A. E. 1985, Ph.D. thesis, University of Maryland.
van den Bergh, S. and Herbst, W. 1975, *A.J.*, **80**, 208.
Verter, F., Magnani, L., Rickard, L. J, and Dwek, E. 1990, in preparation.
Weiland, J. L., Blitz, L., Dwek, E., Hauser, M. G., Magnani, L., and Rickard, L. J 1986, *Ap. J. (Letters)*, **306**, L101.
Winkler, P. F., Tuttle, J. H., Kirshner, R. P., and Irwin, M. J. 1988, in *Supernova Remnants and the Interstellar Medium*, ed. R. S. Roger and T. L. Landecker (Cambridge: Cambridge University Press), p. 65.

RICHARD G. ARENDT and ELI DWEK: Laboratory for Astronomy and Solar Physics, Code 685, NASA/Goddard Space Flight Center, Greenbelt MD 20771

ROBERT PETRE: Laboratory for High Energy Astrophysics, Code 666, NASA/Goddard Space Flight Center, Greenbelt, MD 20771